J. Fluid Mech. (2023), *vol*. 959, A23, doi:10.1017/jfm.2023.153

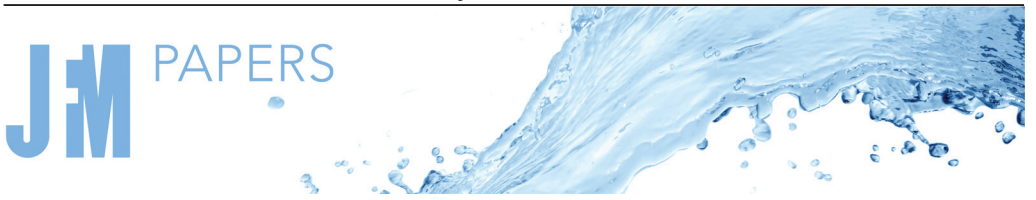

Linear stability of monopolar vortices over isolated topography

Jeasson F. Gonzalez[1] **and L. Zavala Sansón**[1],†

[1]Departamento de Oceanografía Física, CICESE, Carretera Ensenada-Tijuana 3918, 22860, Ensenada, Mexico

(Received 30 July 2022; revised 15 February 2023; accepted 16 February 2023)

The linear instability of circular vortices over isolated topography in a homogeneous and inviscid fluid is examined for the shallow-water and quasi-geostrophic models in the f-plane. The eigenvalue problem associated with azimuthal disturbances is derived for arbitrary axisymmetric topographies, either submarine mountains or valleys. Amended Rayleigh and Fjørtoft theorems with topographic effects are given for barotropic instability, obtaining necessary criteria for instability when the potential vorticity gradient is zero somewhere in the domain. The onset of centrifugal instability is also discussed by deriving the Rayleigh circulation theorem with topography. The barotropic instability theorems are applied to a wide family of nonlinear, quasi-geostrophic solutions of circular vortices over axisymmetric topographic features. Flow instability depends mainly on the vortex/topography configuration, as well as on the vortex size in comparison with the width of the topography. It is found that anticyclones/mountains and cyclones/valleys may be unstable. In contrast, cyclone/mountain and anticyclone/valley configurations are stable. These statements are validated with two numerical methods. First, the generalised eigenvalue problem is solved to obtain the wavenumber of the fastest-growing perturbations. Second, the evolution of the vortices is simulated numerically to detect the development of linear perturbations. The numerical results show that for unstable vortices over narrow topographies, the fastest growth rate corresponds to mode 1, which subsequently forms asymmetric dipolar structures. Over wide topographies, the fastest perturbations are mainly modes 1 and 2, depending on the topographic features.

Key words: quasi-geostrophic flows, topographic effects, vortex instability

1. Introduction

The ocean is a complex physical system due to the interaction of motions of different length and time scales. Nevertheless, long-lived coherent structures in the ocean are discernible in observational data. In particular, mesoscale vortices with typical horizontal scales of the order of 100 km may persist during several weeks or even months.

† Email address for correspondence: lzavala@cicese.mx

The lifetime of such structures is affected by external forcing mechanisms, interactions with other oceanic features, and their intrinsic stability properties. An example is reported by Dewar (2002), who discusses the evolution of meddies (i.e. sub-surface vortices of Mediterranean origin), which are affected by the shape of the seafloor. Careful observations of meddies suggest that interactions with topographic features may be disruptive and lead to vortex disintegration (Shapiro, Meschanov & Emelianov 1995; Richardson & Tychensky 1998). A similar process is observed during the transit of Agulhas eddies over submarine ridges in the south-eastern Atlantic Ocean (Kamenkovich *et al.* 1996; Schouten *et al.* 2000). The obstruction and eventual destruction of vortices encountering topographic obstacles in a rotating system have been studied in laboratory experiments (Zavala Sansón 2002; Zavala Sansón, Barbosa Aguiar & van Heijst 2012) and numerical simulations (e.g. van Geffen & Davies 2000; Zavala Sansón & Gonzalez 2021).

Analytical models of coherent vortices are helpful to understand their general dynamics and stability properties, which can then be compared with realistic conditions. Here, we are interested in nonlinear vortical solutions in a rotating system, which are often used to model persistent structures in the oceans and atmosphere (van Heijst & Clercx 2009). Nonlinearities are a key ingredient that prevents vortex erosion in the form of planetary or topographic Rossby waves, which are generated in the presence of spatial variations of the planetary vorticity (β effect) or bottom topography, respectively. In the quasi-geostrophic (QG) context, a type of dipolar structures is the so-called 'modon' (Stern 1975). Solutions of frontal oceanic eddies in a reduced-gravity model, known as 'rodons', were derived by Cushman-Roisin, Heil & Nof (1985). Azimuthal-mode solutions of multipolar, barotropic and baroclinic QG vortices were derived by Viúdez (2019*a*,*b*). Recently, Gonzalez & Zavala Sansón (2021) obtained nonlinear solutions of monopoles and dipoles over an isolated topographic feature. The latter will be considered in this work to study the stability of monopolar vortices trapped over seamounts and valleys.

The stability of monopolar vortices in a rotating system with no topography has been studied from different points of view. Gent & McWilliams (1986) investigated the linear instability of QG circular vortices with zero circulation in the f-plane to azimuthal normal mode perturbations. The authors found that the fastest growing perturbations may be internal (with vertical structure) or external (barotropic) depending on the steepness of the stream function radial profile. A linearised contour dynamics model, used by Flierl (1988), extended the analysis to baroclinic circular vortices. Rotating tank experiments and three-dimensional numerical simulations have shown that cyclonic and anticyclonic vortices may be subject to both barotropic (two-dimensional) and centrifugal (three-dimensional) instabilities (Kloosterziel & van Heijst 1991; Orlandi & Carnevale 1999). A necessary criterion for barotropic linear instability is obtained from Rayleigh's inflexion point theorem adapted to swirling flows (Gent & McWilliams 1986). The authors found that isolated vortices (circular flows with zero net circulation) may be barotropically unstable and, for sufficiently steep vorticity profiles, develop a wavenumber two azimuthal perturbation transforming into tripolar structures. In rotating tank experiments, unstable cyclonic vortices typically form tripoles (van Heijst & Kloosterziel 1989). Higher wavenumbers leading to multipolar vortices are also possible (Carnevale & Kloosterziel 1994; Trieling, van Heijst & Kizner 2010; Cruz Gómez, Zavala Sansón & Pinilla 2013). Anticyclones, in contrast, are prone to centrifugal instabilities and usually break into dipole pairs (Kloosterziel & van Heijst 1991). The combined effects of barotropic and centrifugal instabilities were discussed thoroughly by Orlandi & Carnevale (1999). On the other hand, non-isolated vortices (with monotonic vorticity profiles) are barotropically stable (Kloosterziel & van Heijst 1992).

Topographic features at the solid bottom can affect vortices with finite depth. Numerical and experimental studies have revealed different physical processes involved in the vortex–topography interactions. These include the radiation of topographic waves and the paths that monopolar and dipolar vortices follow around local topographies, such as seamounts and valleys (Carnevale, Kloosterziel & van Heijst 1991). Oceanic eddies are often eroded or divided when encountering a tall seamount (Herbette, Morel & Arhan 2002, 2005; Sutyrin, Herbette & Carton 2011) or a submarine ridge (van Geffen & Davies 1999; Zavala Sansón 2002). In some cases, vortical structures can be trapped over the topography (Zavala Sansón *et al.* 2012; Zavala Sansón & Gonzalez 2021), and a natural question concerns the stability of such configurations. Carton & Legras (1994) studied the stability of shielded circular vortices over an axisymmetric parabolic bottom, and found that if the vortex core is cyclonic, then a compact and stable tripolar structure emerges. In contrast, the tripoles formed from anticyclonic vortices are unstable and break into two dipoles moving in opposite directions. Nycander & Lacasce (2004) used generalised variational principles to find stable regimes for monopolar barotropic vortices over topography when the potential vorticity profiles are monotonic. In that case, the authors found a large set of stable anticyclonic and cyclonic vortices over a circular seamount. Zhao, Chieusse-Gérard & Flierl (2019) studied the stability of a barotropic Rankine vortex over a cylindrical topography and found that anticyclones are destabilised by seamounts and stabilised by depressions. These results were based on the assumption that the potential vorticity is a piecewise constant function. The jumps in the potential vorticity arose from both the cylindrical topography and the relative vorticity profile. The linear stability of another piecewise circular flow around a rigid cylindrical 'island' with conical topography was studied by Rabinovich, Kizner & Flierl (2018), and the resulting nonlinear evolution by Rabinovich, Kizner & Flierl (2019). In these studies, the authors discuss the stabilising/destabilising role of the bottom slope on clockwise and anticlockwise flows.

This work studies the linear stability of barotropic monopolar vortices over isolated topography. In the first part (§ 2), we pose the problem of a circular flow perturbed by azimuthal normal modes, and derive a generalised eigenvalue problem for the corresponding growth rates. The analysis is carried out for flows under the shallow-water (SW) approximation and extended to the QG dynamics. Then extensions of classical theorems for barotropic and centrifugal instabilities taking topographic effects into account are presented. In the second part (§ 3), we study numerically the stability of circular vortices over axisymmetric topography in the QG limit. The background flow is based on the recent QG solutions obtained by Gonzalez & Zavala Sansón (2021), which represent both cyclones and anticyclones over mountains and valleys, and whose potential vorticity is not uniform. A relevant feature of the solutions is that the bottom topography is arbitrary, subject only to the restriction of being axisymmetric and isolated (the bottom topography becomes flat at large radii). The theoretical results are contrasted with the spectral solution of the corresponding generalised eigenvalue problem. In addition, we perform QG numerical simulations initialised with different vortex–topography configurations. Finally, conclusions are discussed in § 4.

2. Stability of monopolar vortices over axisymmetric topography

2.1. *Linear analysis for SW and QG flows*

This subsection examines the linear stability problem associated with the SW model on the f-plane, including topographic effects and under the rigid-lid approximation.

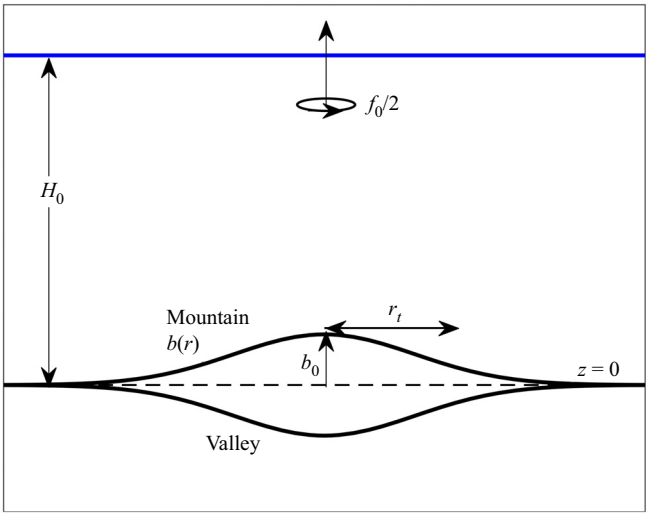

Figure 1. Side view of a fluid layer with mean depth H_0 over bottom topography $b(r)$ defined as an axisymmetric submarine mountain or valley of amplitude b_0 and width r_t on an f-plane.

Using polar coordinates (r, θ) and assuming an axisymmetric topography, a single fluid layer in this system satisfies the vorticity equation

$$h_s \frac{\partial q_s}{\partial t} + J(\psi_s, q_s) = 0, \tag{2.1}$$

where ψ_s represents the transport function, and $q_s = h_s^{-1}(\omega_s + f_0)$ is the potential vorticity (PV), with $\omega_s = \nabla \cdot (h_s^{-1} \nabla \psi_s)$ the relative vorticity, and f_0 the Coriolis parameter. Also, $J(a, b) = (\partial_r a\, \partial_\theta b - \partial_\theta a\, \partial_r b)/r$ is the Jacobian operator, and $h_s(r) = H_0 - b(r)$ is the fluid layer thickness, where $b(r)$ is the axisymmetric topographic profile with amplitude b_0 and horizontal scale r_t, and H_0 is the average depth of the fluid layer (figure 1). We consider isolated topographies, $\mathrm{d}b/\mathrm{d}r \to 0$ for $r \gg r_t$, which can be mountains ($b_0 > 0$) or valleys ($b_0 < 0$). Under the rigid-lid approximation, the temporal variations of the layer thickness are ignored in the continuity equation, so surface gravity waves are suppressed. The radial and azimuthal velocity components are defined as $u_s = -(h_s r)^{-1}\, \partial_\theta \psi_s$ and $v_s = h_s^{-1}\, \partial_r \psi_s$.

A linear stability analysis is used to introduce small, two-dimensional disturbances $\psi_s'(r, \theta, t)$ on a basic flow $\Psi_s(r)$, which represents a steady, axisymmetric solution of (2.1):

$$\psi_s(r, \theta, t) = \Psi_s(r) + \psi_s'(r, \theta, t). \tag{2.2}$$

The basic flow can be a circular cyclonic or anticyclonic vortex swirling above the topography, which can be a mountain or a valley. Note that the potential vorticity can be written as

$$q_s(r, \theta, t) = Q_s(r) + q_s'(r, \theta, t), \tag{2.3}$$

where $Q_s = h_s^{-1}[\nabla \cdot (h_s^{-1} \nabla \Psi_s) + f_0]$ is the basic PV, and $q_s' = h_s^{-1} \nabla \cdot (h_s^{-1} \nabla \psi_s')$ is its perturbation. Inserting (2.2) and (2.3) into the vorticity equation (2.1) and linearising:

$$h_s \frac{\partial q_s'}{\partial t} + J(\Psi_s, q_s') + J(\psi_s', Q_s) = 0. \tag{2.4}$$

The disturbance is assumed of the form

$$\left.\begin{aligned}\psi_s'(r,\theta,t) &= \phi(r)\,\mathrm{e}^{\mathrm{i}(k\theta-\sigma t)},\\ q_s'(r,\theta,t) &= \frac{1}{h_s}\,\mathcal{L}_s[\phi(r)]\,\mathrm{e}^{\mathrm{i}(k\theta-\sigma t)},\end{aligned}\right\} \tag{2.5}$$

where $\mathcal{L}_s[\ ]$ is a differential operator defined by $\mathcal{L}_s = r^{-1}\,\partial_r(rh_s^{-1}\,\partial_r) - r^{-2}h_s^{-1}k^2$, k is the azimuthal wavenumber, $\phi(r)$ is a complex amplitude, and $\sigma = \sigma_r + \mathrm{i}\sigma_i$ is a complex number whose real part is the frequency of the disturbance, and the imaginary part represents its growth rate. The condition for instability is that the growth rate σ_i is positive.

Applying (2.5) to (2.4) provides the generalised eigenvalue problem

$$\sigma\,\mathcal{L}_s\phi = \frac{k}{r}\left[\frac{\partial_r\Psi_s}{h_s}\,\mathcal{L}_s - \partial_r Q_s\right]\phi. \tag{2.6}$$

The matrix representation of this equation is given by

$$\sigma\boldsymbol{A}\,\phi(r) = \boldsymbol{B}\,\phi(r), \tag{2.7}$$

where $\boldsymbol{A}$ and $\boldsymbol{B}$ are non-Hermitian and real matrices, σ is the eigenvalue, and ϕ is the eigenfunction. Solutions of (2.6) for different wavenumbers k provide the eigenvalues and, consequently, the growth rate of the corresponding perturbation. However, analytical solutions are often difficult to obtain, so the problem is usually solved numerically, as we will do in § 3.

Now we examine the QG dynamics obtained when the layer thickness is much greater than the amplitude of the topography, $H_0 \gg b_0$ (Vallis 2017). In this case, the vorticity equation is

$$\frac{\partial}{\partial t}\nabla^2\psi + J(\psi, q) = 0, \tag{2.8}$$

where now $\psi = \psi_s/H_0$ is the stream function, and $q = \omega + h(r)$ is the QG PV, with $\omega = \nabla^2\psi$ the relative vorticity, and $h(r) = f_0H_0^{-1}\,b(r)$ the ambient vorticity (Zavala Sansón & van Heijst 2014). The radial and azimuthal velocity components are now defined as $u = -r^{-1}\,\partial_\theta\psi$ and $v = \partial_r\psi$, respectively.

The perturbed flow is of the form

$$\psi(r,\theta,t) = \Psi(r) + \psi'(r,\theta,t), \tag{2.9}$$

where Ψ $(= \Psi_s/H_0)$ is the basic flow, and ψ' is a small perturbation. Applying the same linear analysis used for the SW equations, we obtain the generalised eigenvalue problem

$$\sigma\,\mathcal{L}\phi = \frac{k}{r}\,[\partial_r\Psi\,\mathcal{L} - \partial_r(\nabla^2\Psi + h)]\phi, \tag{2.10}$$

where the linear operator is $\mathcal{L} = \partial_{rr} + r^{-1}\,\partial_r - r^{-2}k^2$. This expression for QG can be compared with the SW version (2.6).

2.2. *Barotropic instability*

Barotropic instability refers to growing disturbances that arise on shear flows. A necessary criterion for instability is provided by Rayleigh's inflexion point theorem for either parallel or circular two-dimensional flows (Gent & McWilliams 1986). A more restrictive (yet necessary) criterion is given by Fjørtoft's theorem. This subsection presents a new version of these theorems for circular vortices over topography.

2.2.1. *Rayleigh's inflexion point theorem with topography*

The generalised eigenvalue problem (2.6) in the SW model can provide an equivalent of Rayleigh's inflexion point theorem involving topography effects. First, (2.6) is rewritten as

$$\frac{\mathrm{d}}{\mathrm{d}r}\left(\frac{r}{h_s}\frac{\mathrm{d}\phi}{\mathrm{d}r}\right)-\frac{k^2}{rh_s}\phi-\frac{d_rQ_s}{r^{-1}h_s^{-1}\,d_r\Psi_s-\sigma/k}\phi=0, \tag{2.11}$$

where $d_r \equiv \mathrm{d}/\mathrm{d}r$. Note that (2.11) assumes $r^{-1}h_s^{-1}\,d_r\Psi_s-\sigma/k\neq 0$ to avoid trivial solutions of ϕ (because $d_rQ_s\neq 0$ in general). Multiplying this equation by the complex conjugate ϕ^*, integrating each term, and applying the null boundary conditions at $r=0$ and $r=r_m\to\infty$ (the maximum value in the radial direction), both obtained from the asymptotic analysis for small and large r (Gent & McWilliams 1986), yields

$$\int_0^{r_m}\frac{r}{h_s}\,|d_r\phi|^2\,\mathrm{d}r+\int_0^{r_m}\frac{k^2}{rh_s}\,|\phi|^2\,\mathrm{d}r+\int_0^{r_m}\frac{(r^{-1}h_s^{-1}\,d_r\Psi_s-\sigma^*/k)\,d_rQ_s}{|r^{-1}h_s^{-1}\,d_r\Psi_s-\sigma/k|^2}\,|\phi|^2\,\mathrm{d}r=0. \tag{2.12}$$

The imaginary part of (2.12) is

$$\frac{\sigma_i}{k}\int_0^{r_m}\frac{d_rQ_s}{|r^{-1}h_s^{-1}\,d_r\Psi_s-\sigma/k|^2}\,|\phi|^2\,\mathrm{d}r=0. \tag{2.13}$$

If $\sigma_i\neq 0$, then the basic flow could be unstable. In this case, to satisfy (2.13), the potential vorticity gradient must be zero at some $r=r_z$, i.e.

$$\frac{\mathrm{d}}{\mathrm{d}r}\left[\frac{\boldsymbol{\nabla}\cdot(h_s^{-1}\,\boldsymbol{\nabla}\Psi_s)+f_0}{h_s}\right]\Bigg|_{r=r_z}=0, \tag{2.14}$$

which is a necessary criterion of instability for the SW model. In the QG limit, the result is equivalent but now using the QG PV:

$$\frac{\mathrm{d}}{\mathrm{d}r}[\nabla^2\Psi+h(r)]\Big|_{r=r_z}=0. \tag{2.15}$$

Note that for the flat-bottom case, $h(r)=0$, condition (2.15) demands the relative vorticity gradient to be null at some radial distance, as reported by Gent & McWilliams (1986).

2.2.2. *Fjørtoft's theorem with topography*

Here, we present an equivalent criterion of Fjørtoft's theorem with topography in the SW model. First, note that the real part of (2.12) allows us to find

$$\int_0^{r_m}\frac{d_rQ_s\,(r^{-1}h_s^{-1}\,d_r\Psi_s-\sigma_r/k)}{|r^{-1}h_s^{-1}\,d_r\Psi_s-\sigma/k|^2}\,|\phi|^2\,\mathrm{d}r<0. \tag{2.16}$$

Second, if $\sigma_i\neq 0$ and condition (2.13) is satisfied, then

$$(r^{-1}h_s^{-1}\,d_r\Psi_s|_{r=r_z}-\sigma_r/k)\int_0^{r_m}\frac{d_rQ_s}{|r^{-1}h_s^{-1}d_r\,\Psi_s-\sigma/k|^2}\,|\phi|^2\,\mathrm{d}r=0. \tag{2.17}$$

Subtracting (2.17) from (2.16), we obtain

$$\int_0^{r_m}\frac{d_rQ_s\,(r^{-1}h_s^{-1}\,d_r\Psi_s-r^{-1}h_s^{-1}\,d_r\Psi_s|_{r=r_z})}{|r^{-1}h_s^{-1}\,d_r\Psi_s-\sigma/k|^2}\,|\phi|^2\,\mathrm{d}r<0, \tag{2.18}$$

which, to be satisfied, requires that the numerator of the integrand be negative for some r:

$$\frac{\mathrm{d}}{\mathrm{d}r}\left[\frac{\boldsymbol{\nabla}\cdot(h_s^{-1}\,\boldsymbol{\nabla}\Psi_s)+f_0}{h_s}\right]\left(\frac{1}{rh_s}\,\frac{\mathrm{d}\Psi_s}{\mathrm{d}r}-\frac{1}{r_z\,h_s(r_z)}\,\frac{\mathrm{d}\Psi_s}{\mathrm{d}r}\bigg|_{r=r_z}\right)<0. \tag{2.19}$$

This expression indicates that circular flow over topography could be unstable if the sign of the velocity relative to the inflexion point is opposite to the sign of the potential vorticity derivative somewhere.

In the QG approximation, the instability criterion (2.19) is rewritten as

$$\frac{\mathrm{d}}{\mathrm{d}r}[\nabla^2\Psi+h(r)]\left(\frac{1}{r}\,\frac{\mathrm{d}\Psi}{\mathrm{d}r}-\frac{1}{r_z}\,\frac{\mathrm{d}\Psi}{\mathrm{d}r}\bigg|_{r=r_z}\right)<0. \tag{2.20}$$

When there is no topography, $h(r)=0$, (2.20) is reduced to the theorem reported by Gent & McWilliams (1986) for circular flow. Notice that Fjørtoft's theorem (2.20) requires that the point $r=r_z$, where Rayleigh's theorem is satisfied, exists.

2.3. *Centrifugal instability*

Vertical motions in a three-dimensional swirling flow are able to trigger centrifugal instabilities (Orlandi & Carnevale 1999). Rayleigh's circulation theorem provides a criterion to identify this type of instability (Kloosterziel & van Heijst 1991). The criterion is based on energetic considerations for an axisymmetric flow with an arbitrary azimuthal velocity $v(r)$ in the absence of viscosity, stratification and rotation, and with a flat bottom. An extension of the theorem including rotation effects was presented in Kloosterziel (1990) and Kloosterziel & van Heijst (1991), based on the conservation of angular momentum of fluid elements subjected to infinitesimal displacements. By following a similar analytical procedure, in this subsection we present an extension of the circulation theorem including topography effects. Note that centrifugal instability is inherently three-dimensional, in contrast with the purely two-dimensional barotropic instability examined above.

Consider the momentum equations of a circularly symmetric flow in cylindrical coordinates (r,θ,z) on the f-plane:

$$\frac{\mathrm{D}u}{\mathrm{D}t}-f_0v-\frac{v^2}{r}=-\frac{1}{\rho}\,\frac{\partial P}{\partial r}, \tag{2.21}$$

$$\frac{\mathrm{D}v}{\mathrm{D}t}+f_0u+\frac{uv}{r}=0, \tag{2.22}$$

$$0=-\frac{1}{\rho}\,\frac{\partial P}{\partial z}-g, \tag{2.23}$$

where (u,v) are the radial and azimuthal velocity components, $P(r,z)$ is the pressure, g is gravity, and $D/Dt=\partial/\partial t+u\,\partial/\partial r+w\,\partial/\partial z$ is the material derivative, with w the vertical velocity. The pressure is θ-independent because the flow maintains its circular shape. The flow is assumed to maintain the hydrostatic balance in the vertical direction (as in the SW approximation).

Now consider the presence of the axisymmetric topography $b(r)$ shown in figure 1. Integrating (2.23) from an arbitrary level z and the surface, the pressure is

$$P=\rho g[h_s(r)+b(r)]-\rho gz. \tag{2.24}$$

The first term, $p(r)=\rho g\,h_s(r)$, is the pressure associated with the surface elevation (which is neglected only in the continuity equation under the rigid-lid approximation).

The horizontal momentum equations are rewritten as

$$\frac{\mathrm{D}u}{\mathrm{D}t} = \frac{v^2}{r} + f_0 v - \frac{1}{\rho}\frac{\mathrm{d}p}{\mathrm{d}r} - g\frac{\mathrm{d}b}{\mathrm{d}r}, \tag{2.25}$$

$$\frac{\mathrm{D}}{\mathrm{D}t}\left(vr + \frac{1}{2}f_0 r^2\right) = 0, \tag{2.26}$$

where (2.26) represents the conservation of absolute angular momentum.

As a basic flow, we assume a circular monopolar vortex with azimuthal velocity $v(r)$. Following Kloosterziel & van Heijst (1991), we consider a fluid element that is displaced from $r = r_0$ to $r' = r_0 + \delta r$ without changing the pressure field $p(r)$ (in this sense the displacement is considered as virtual). The new azimuthal velocity is $v'(r')$. Using the conservation law (2.26) yields

$$v'(r')\, r' + \tfrac{1}{2} f_0 r'^2 = v(r_0)\, r_0 + \tfrac{1}{2} f_0 r_0^2. \tag{2.27}$$

The radial acceleration due to the virtual displacement is obtained from (2.25) as the variation of the acceleration between both states (disturbed and basic) evaluated at r':

$$\frac{\mathrm{D}^2\delta r}{\mathrm{D}t^2} = \left(\frac{\mathrm{D}u'}{\mathrm{D}t} - \frac{\mathrm{D}u}{\mathrm{D}t}\right)\bigg|_{r=r'}. \tag{2.28}$$

Using (2.25), and after some manipulations,

$$\begin{aligned}\frac{\mathrm{D}^2\delta r}{\mathrm{D}t^2} &= \left[\frac{v'(r')^2}{r'} + f_0\, v'(r') - \frac{v(r')^2}{r'} - f_0\, v(r')\right] - g\delta\frac{\mathrm{d}b}{\mathrm{d}r} \\ &= \frac{1}{r'^3}\left[\left(v'(r')\, r' + \frac{1}{2}f_0 r'^2\right)^2 - \left(v(r')\, r' + \frac{1}{2}f_0 r'^2\right)^2\right] - g\delta\frac{\mathrm{d}b}{\mathrm{d}r}.\end{aligned} \tag{2.29}$$

Here, $\delta\, \mathrm{d}b/\mathrm{d}r = \mathrm{d}b/\mathrm{d}r|_{r'} - \mathrm{d}b/\mathrm{d}r|_{r_0}$ is the variation of the topography gradient as the particle is displaced. Substituting the first term with (2.27) gives

$$\frac{\mathrm{D}^2\delta r}{\mathrm{D}t^2} = \frac{1}{r'^3}\left[\left(v(r_0)\, r_0 + \frac{1}{2}f_0 r_0^2\right)^2 - \left(v(r')\, r' + \frac{1}{2}f_0 r'^2\right)^2\right] - g\delta\frac{\mathrm{d}b}{\mathrm{d}r}. \tag{2.30}$$

A Taylor expansion close to r_0 simplifies this expression to order δr:

$$\frac{\mathrm{D}^2\delta r}{\mathrm{D}t^2} \sim -\delta r\frac{\mathrm{d}}{\mathrm{d}r}\left[\frac{1}{r_0^3}\left(v(r)\, r + \frac{1}{2}f_0 r^2\right)^2 + g\frac{\mathrm{d}}{\mathrm{d}r}b(r)\right]_{r=r_0}. \tag{2.31}$$

If the fluid element is displaced outwards ($\delta r > 0$), then the acceleration (2.31) in that direction is positive when

$$\frac{\mathrm{d}}{\mathrm{d}r}\left[\frac{1}{r_0^3}\left(v(r)\, r + \frac{1}{2}f_0 r^2\right)^2 + g\frac{\mathrm{d}}{\mathrm{d}r}b(r)\right]_{r=r_0} < 0. \tag{2.32}$$

Or, taking the derivative,

$$\frac{2}{r_0}\left(v(r_0) + \frac{1}{2}f_0 r_0\right)(\omega(r_0) + f_0) + g\frac{\mathrm{d}^2}{\mathrm{d}r^2}b(r_0) < 0, \tag{2.33}$$

with the vorticity $\omega(r) = d_r[r\, v(r)]/r$. The same condition applies for an inward displacement $\delta r < 0$ and a negative acceleration. Thus (2.33) is a sufficient criterion for

centrifugal instability. Scaling (2.33), we obtain the dimensionless criterion

$$\frac{1}{r_a}(\epsilon v_a + r_a)(\epsilon\omega_a + 2) + 2\Delta\left(\frac{L_D}{L}\right)^2 \frac{\mathrm{d}^2 b_a}{\mathrm{d}r_a^2} < 0, \tag{2.34}$$

where $(\,)_a$ represents dimensionless variables, $\epsilon = 2U/Lf_0$ is the Rossby number based on the horizontal length L, the velocity scale U and the system's angular speed $f_0/2$, $L_D = \sqrt{gH_0}/f_0$ is the deformation radius based on the mean depth, and $\Delta = b_0/H_0$ is the normalised topographic amplitude (to be used later). Notice that the first term in (2.34) corresponds to the circulation theorem reported by Kloosterziel & van Heijst (1991) for a flat bottom, $b_0 = 0$. The new condition extends Rayleigh's circulation theorem involving topography effects. The criterion applies for SW flows and also in the QG limit, in which b_0 is restricted to be much smaller than the average depth H_0.

The stability criterion (2.34) indicates that the shape of the topography and the vortex size are essential. The shape establishes the sign of $\mathrm{d}^2 b/\mathrm{d}r^2$; for example, a topography without inflexion point in its skirt, as is the case for a hemispherical topography, has a second derivative with only one sign, negative for a mountain or positive for a valley. Thus the hemispherical mountain (valley) tends to destabilise (stabilise) the vortex stable (unstable) over the flat bottom. A more realistic topographic shape would have at least one inflexion point, as in a Gaussian profile, so instabilities may develop depending on the radial distance at which the flow is disturbed. On the other hand, for a 'small' vortex in the SW dynamics ($\Delta \sim O(1)$ and $L < L_D$ but still within the mesoscale), the topographic contribution is more relevant in the centrifugal instability than for 'big' vortices ($L > L_D$). In QG, $L \sim L_D$ and $\Delta \ll 1$, so the topographic term is less important.

3. Stability analyses of QG vortices over topography

In this section, we discuss the stability criteria for a special class of QG monopolar vortices over arbitrary axisymmetric topography derived recently by Gonzalez & Zavala Sansón (2021). These nonlinear solutions of (2.8) represent a versatile family of cyclonic and anticyclonic vortices over mountains and valleys on the f-plane. The analytical vortical solutions support the notion that long-lived motions may exist over topographic features, as often occurs in the oceans, rotating tank experiments and numerical simulations (see § 1 and references therein). Despite the strong simplifications (circular flows over axisymmetric topography), the relevance of analytical solutions is that they allow one to test the barotropic instability theorems discussed in § 2. Also, exact solutions are a suitable initial condition in numerical simulations, as we will see below.

3.1. *Vortices over an isolated topography: the basic flow*

The analytical solutions reported by Gonzalez & Zavala Sansón (2021) are steady structures based on azimuthal modes adapted to the shapes of mountains and valleys. The flows discussed here correspond to monopolar vortices with azimuthal mode $m = 0$, and stream function amplitude $\hat{\psi}$, whose sign corresponds to either anticyclonic ($\hat{\psi} > 0$) or cyclonic ($\hat{\psi} < 0$) vortices. The arbitrary topographic profile is chosen Gaussian, $b(r) = b_0\,\mathrm{e}^{-r^2/r_t^2}$, where b_0 is the mountain (valley) height (depth), and r_t is the width of the topography (see figure 1).

The solutions are a family of piecewise functions depending on the topographic parameters. Scaling the radial coordinate as $s = c_0 r$, with c_0 a factor with units 1/length, the non-dimensional forms of the stream function $\Psi_a(s)$, the azimuthal velocity

$v_a(s) = d_s\Psi_a$, and the relative vorticity $\omega_a(s) = s^{-1}\, d_s(sv_a)$ (where d_s is the dimensionless radial derivative) are

$$\Psi_a(s) = \frac{\Psi}{\hat{\psi}} = \begin{cases} \Psi_I(s;\, \xi_t,\, s_t) - a_0(\xi_t,\, s_t) - a_2(\xi_t,\, s_t)\, s^2, & s \le s_l, \\ a_1(\xi_t,\, s_t)\ln s, & s \ge s_l, \end{cases} \tag{3.1}$$

$$v_a(s) = \frac{v}{c_0\hat{\psi}} = \begin{cases} d_s\Psi_I(s;\, \xi_t,\, s_t) - 2a_2(\xi_t,\, s_t)\, s, & s \le s_l, \\ a_1(\xi_t,\, s_t)/s, & s \ge s_l, \end{cases} \tag{3.2}$$

$$\omega_a(s) = \frac{\omega}{c_0^2\hat{\psi}} = \begin{cases} -\Psi_I(s;\, \xi_t,\, s_t) + \xi_t\, H(s;\, s_t) - 4a_2(\xi_t,\, s_t), & s \le s_l, \\ 0, & s \ge s_l. \end{cases} \tag{3.3}$$

The core of the vortex is centred at the topography in a circular interior region of radius s_l, chosen as the first zero of the order 1 Bessel function ($s_l = 3.8317$). The exterior region $s \ge s_l$ consists of a potential flow. The coefficients a_i ($i = 0,\, 1,\, 2$) are used to guarantee the continuity of the flow variables (see Appendix A). The axisymmetric functions $\Psi_I(s;\, \xi_t,\, s_t)$ and $H(s;\, s_t)$ (defined below), as well as the constants a_i, depend on the dimensionless parameters

$$\xi_t = \frac{h_0}{c_0^2\hat{\psi}} \equiv \frac{\Delta}{Ro}, \quad s_t = c_0 r_t. \tag{3.4a,b}$$

The first is the ratio between the ambient vorticity at the origin, $h_0 \equiv h(0) = f_0 b_0/H_0$, and the vorticity scale, $c_0^2\hat{\psi}$. Note that ξ_t is equivalent to the ratio between the relative topographic amplitude $\Delta = b_0/H_0$ and the Rossby number based on the Coriolis parameter, $Ro = c_0^2\hat{\psi}/f_0$ (and hence $\epsilon = 2\,Ro$ in the circulation theorem (2.34)). The second parameter, s_t, is the dimensionless horizontal scale of the topography. Hereafter we will refer to 'narrow' topographies when $s_t < s_l$, that is, the horizontal scale of the mountain or valley is shorter than the vortex scale. Similarly, a 'wide' topography means $s_t > s_l$.

The explicit expression for the topographic function H is

$$H(s;\, s_t) = 1 - \mathrm{e}^{-(s^2/s_t^2)}, \tag{3.5}$$

while the stream function Ψ_I, and $d_s\Psi_I$ in the interior region, are given by

$$\Psi_I(s;\, \xi_t,\, s_t) = J_0(s) + \xi_t\left(\frac{\pi}{2}\, Y_0(s)\int_0^s H(s';\, s_t)\, J_0(s')\, s'\, \mathrm{d}s' - \frac{\pi}{2}\, J_0(s)\int_0^s H(s';\, s_t)\, Y_0(s')\, s'\, \mathrm{d}s'\right), \tag{3.6}$$

$$d_s\Psi_I(s;\, \xi_t,\, s_t) \equiv v_I(s;\, \xi_t,\, s_t) = -J_1(s) + \xi_t\left(-\frac{\pi}{2}\, Y_1(s)\int_0^s H(s';\, s_t)\, J_0(s')\, s'\, \mathrm{d}s' + \frac{\pi}{2}\, J_1(s)\int_0^s H(s';\, s_t)\, Y_0(s')\, s'\, \mathrm{d}s'\right), \tag{3.7}$$

where J_0 and Y_0 are the order 0 Bessel functions of the first and second kind, respectively. Note that the divergence of Y_m is avoided because $H(s) \to 0$ at $s \to 0$. Function $v_I(s)$ defined in (3.7) will be used later. After some calculations, it is verified that the potential vorticity is proportional to Ψ_I, so that $q_a \equiv \omega_a + \xi_t\, \mathrm{e}^{-(s^2/s_t^2)} = -\Psi_I + \xi_t - 4a_2$.

A special feature of the QG solutions (3.1) is the symmetry between the signs of the vortex and topography amplitudes, both contained in parameter ξ_t. Specifically, an

Configuration	Identifier	Vortex	Topography	$\xi_t = \Delta/Ro$
Anticyclone/mountain	A/M	$\hat{\psi} > 0$	$b_0 > 0$	$\xi_t > 0$
Cyclone/valley	C/V	$\hat{\psi} < 0$	$b_0 < 0$	
Anticyclone/valley	A/V	$\hat{\psi} > 0$	$b_0 < 0$	$\xi_t < 0$
Cyclone/mountain	C/M	$\hat{\psi} < 0$	$b_0 > 0$	

Table 1. Outline of the flow/topography configurations in the analytical solutions of circular vortices (with cyclonic or anticyclonic amplitude $\hat{\psi}$) over topography (with height or depth b_0).

anticyclone ($\hat{\psi} > 0$) over a mountain ($b_0 > 0$) is equivalent to a cyclone ($\hat{\psi} < 0$) over a valley ($b_0 < 0$). Analogously, the case of a cyclone over a mountain is equivalent to an anticyclone over a valley. For quick reference, the flow/topography configurations are summarised in table 1.

Figure 2 presents several velocity and vorticity radial profiles of the anticyclone/mountain case, $\xi_t > 0$. When the topography is narrow (figures 2*a*,*b*), both profiles change sign at a certain radius (except for the flat topography $\xi_t = 0$). The vorticity profiles indicate that the negative core of the vortex is shielded by a ring of opposite vorticity that becomes zero at s_l. In general, the vortices are not isolated because the total circulation (the area integral of the vorticity) is evidently different from zero. For a wide topography (figures 2*c*,*d*), the azimuthal velocity reaches a maximum at a certain radius and then decays slowly, as in typical vortex models (see e.g. van Heijst & Clercx 2009). In addition, there is also a weak opposite-sign vorticity ring surrounding the vortex core (figure 2*d*).

Figure 3 shows the velocity and vorticity profiles obtained for the cyclone/mountain case $\xi_t < 0$ (equivalent to the anticyclone/valley system). Panels (*a*) and (*c*) indicate no changes in the azimuthal velocity sign for narrow and wide topographies. The signs of the vorticity profiles do not change either (panels *b*,*d*). However, with the increase of ξ_t, the vorticity at the periphery is more intense than at the origin.

We will now evaluate the theorems obtained in subsections §§ 2.2 and 2.3 for the basic flow presented in this subsection.

3.2. *Conditions for barotropic instability: Rayleigh's theorem*

Using solutions (3.1)–(3.3), the dimensionless form of Rayleigh's theorem (2.15) can be rewritten as

$$d_s[\omega_a(s;\xi_t,s_t)+\xi_t(1-H(s;s_t))] \equiv \begin{cases} -v_I(s;\xi_t,s_t)=0, & s \le s_l, \\ -\xi_t\, d_s H(s,s_t)=0, & s \ge s_l, \end{cases} \tag{3.8}$$

where $v_I = d_s\Psi_I$ was defined in (3.7). Consider the following cases for narrow and wide topographies. If the topography becomes flat at the outer region, $d_sH(s;s_t) \equiv 0$ (narrow topography), then the theorem requires that

$$v_I|_{s_{in}} = 0 \tag{3.9}$$

at some $s_{in} < s_l$ in the interior region. Figures 4(*a*,*b*) present the radial profiles of $v_I(s)$ for positive and negative ξ_t values with $s_t = 2$. Vortices with $\xi_t > 0$ (figure 4(*a*) satisfy (3.9) because the sign of $v_I(s)$ changes somewhere in the interior region. Therefore, the A/M

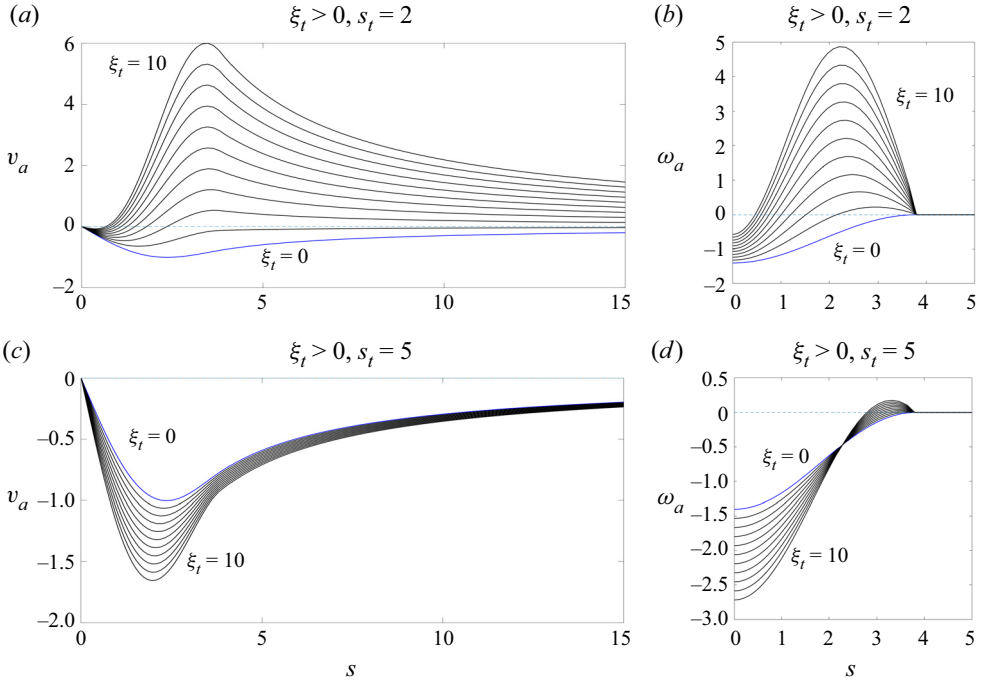

Figure 2. (*a*) Azimuthal velocity and (*b*) relative vorticity profiles, for several antyciclone/mountain (A/M) cases over a narrow topography, $s_t = 2$. (*c*,*d*) Corresponding profiles for a wide topography, $s_t = 5$. The blue curves indicate the flat-bottom cases, $\xi_t = 0$.

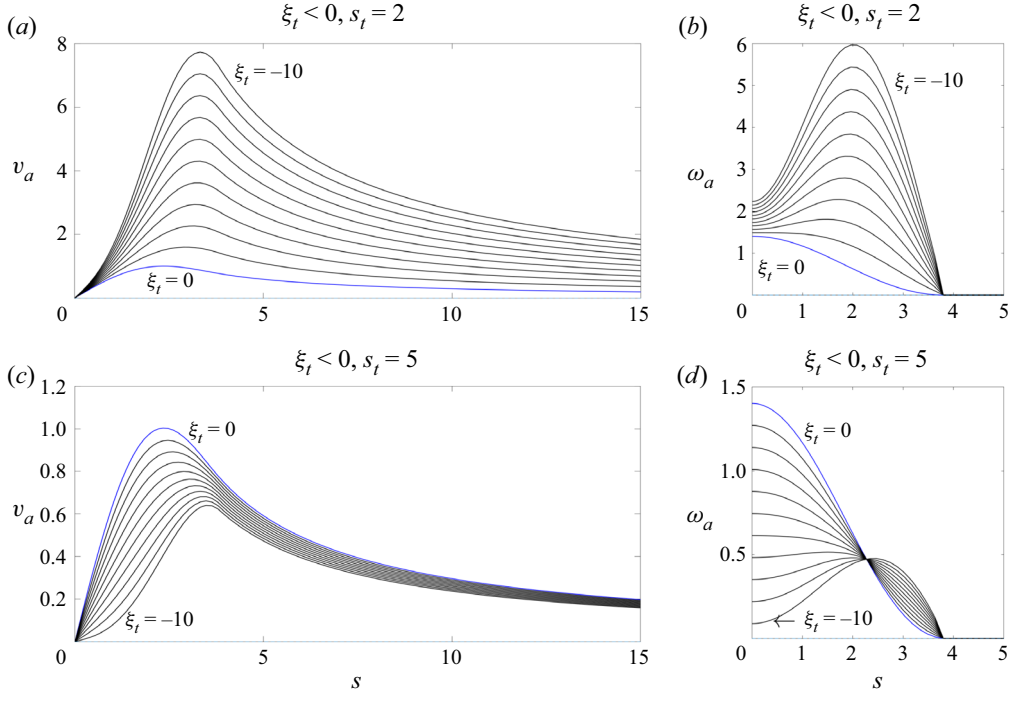

Figure 3. Same as in figure 2, but now for cyclone/mountain (C/M) cases.

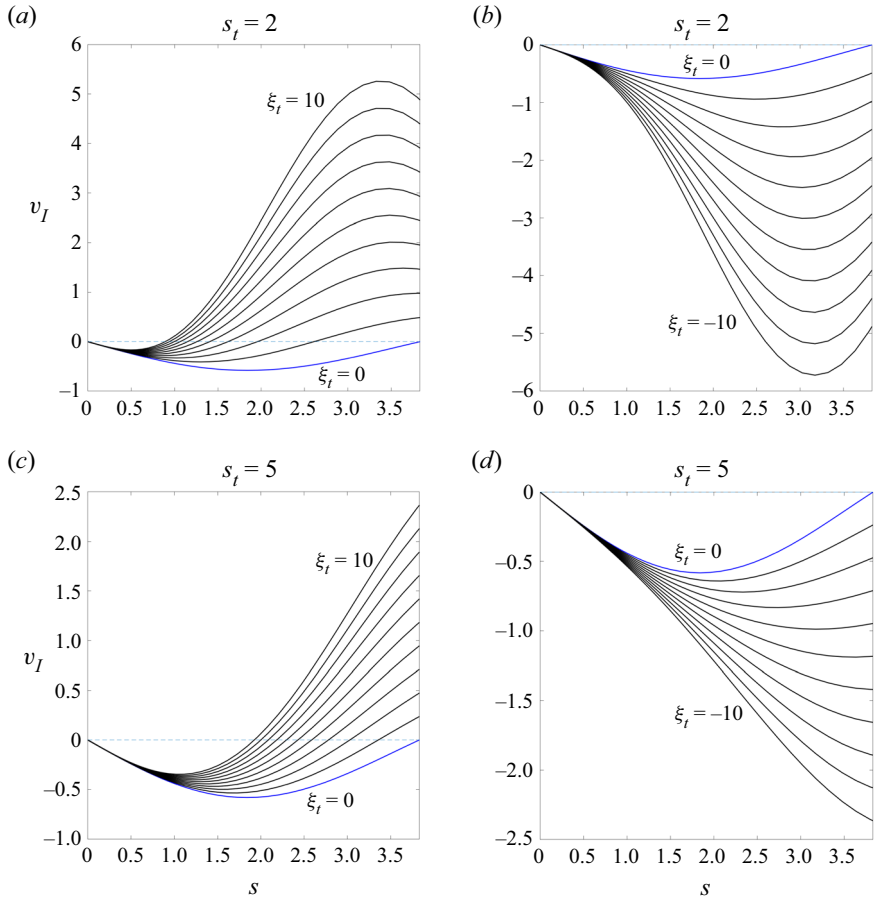

Figure 4. Profiles of the radial function v_I used to evaluate Rayleigh's inflexion point theorem for narrow topography $s_t = 2$: (*a*) $\xi_t > 0$, and (*b*) $\xi_t < 0$. (*c*,*d*) Corresponding profiles for a wide topography $s_t = 5$.

and C/V configurations may be barotropically unstable. Conversely, the velocity fields, corresponding to the cases where $\xi_t < 0$ (figure 4(*b*), do not satisfy (3.9) because $v_I(s) > 0$ everywhere. Thus the C/M and A/V cases are neutrally stable.

When $d_s H(s; s_t) \neq 0$ in the outer region (wide topographies), the vortex might be unstable for the following situation. If $d_s H(s; s_t)$ is of definite sign, then (3.8) is satisfied if $v_I(s; \xi_t, s_t)$ is of opposite sign to $\xi_t\, d_s H(s; s_t)$ in some region, that is,

$$v_I|_{s_{in}} \begin{cases} > 0 & \text{if } \xi_t\, d_s H(s; s_t) < 0, \\ < 0 & \text{if } \xi_t\, d_s H(s; s_t) > 0, \end{cases} \tag{3.10}$$

where $s_{in} < s_l$. In the particular case of Gaussian topography, these relations apply because $d_s H(s; s_t) > 0$ (< 0) for a mountain (valley). Figures 4(*c*,*d*) present the radial profile of $v_I(s)$ for positive and negative ξ_t values with $s_t = 5$. The A/M and C/V configurations in figure 4(*c*) may be unstable because they satisfy the second inequality in (3.10). In contrast, the C/M and A/V cases shown in figure 4(*d*) do not satisfy the first inequality in (3.10), and hence are stable.

Summarising, configurations with $\xi_t > 0$ may be unstable, and those with $\xi_t < 0$ are stable for any topography.

3.3. *Conditions for barotropic instability: Fjørtoft's theorem*

Now we will evaluate criterion (2.20) for our basic flow. We consider only configurations with $\xi_t > 0$ and narrow topographies where Rayleigh's criterion (3.9) is satisfied, that is, $d_s H(s; s_t) = 0$ at the outer region (see figure 4*a*). In these cases, the dimensionless Fjørtoft's theorem (2.20) states that the following inequality should be satisfied simultaneously with Rayleigh's theorem for some s:

$$\gamma_F \equiv v_I(s; \xi_t, s_t)\left(\frac{1}{s}\, v_I(s; \xi_t, s_t) - \frac{1}{s_{in}}\, v_I(s_{in}; \xi_t, s_t)\right) > 0 \quad \text{for } s < s_l, \tag{3.11}$$

where we have used the fact that $d_s q_a = -d_s \psi_I = -v_I$. From (3.9), we know that $v_I(s_{in}; \xi_t, s_t) = 0$, so we can conclude that γ_F satisfies Fjørtoft's theorem because

$$\gamma_F = v_I^2(s; \xi_t, s_t)/s \tag{3.12}$$

is always definite positive.

3.4. *Conditions for centrifugal instability*

Finally, the circulation theorem (2.34) is evaluated for our circular vortices over topography. Recalling that $\epsilon = 2\,Ro = 2\Delta/\xi_t$, we obtain the necessary instability criterion if, for some s,

$$\frac{2}{s}\left(\frac{\Delta}{\xi_t}\, v_a(s; \xi_t, s_t) + \frac{s}{2}\right)\left(\frac{\Delta}{\xi_t}\, \omega_a(s; \xi_t, s_t) + 1\right) + \Delta\left(\frac{L_D}{L}\right)^2 \frac{\mathrm{d}^2}{\mathrm{d}s^2} b_a(s; s_t) < 0. \tag{3.13}$$

Figure 5 shows a set of parameter space maps Ro versus Δ for different Gaussian topographies with horizontal scale s_t. The colours represent logical values for the condition (3.13), where blue indicates false (the configuration does not satisfy Rayleigh's circulation theorem), and red means true values (the configuration does satisfy the theorem, therefore the flow is unstable). In general, the configurations with anticyclones shown in the upper quadrants tend to be centrifugally unstable (red areas).

3.5. *Numerical solution of the generalised eigenvalue problem*

The linear stability analysis for monopolar vortices over topography presented in § 2 led us to obtain the generalised eigenvalue problem (see (2.7) and (2.10)) involving the real matrixes $\boldsymbol{A}$ (without dependence on physical parameters) and $\boldsymbol{B}$ (depending on all physical parameters and the properties of the basic flow). The non-dimensional form of the eigenvalue problem for the circular vortices introduced in 3.1 is given by

$$\frac{\sigma_a}{k}\, \nabla^2_{ka} \zeta_a = \left[\frac{1}{s}\, v_a\, \nabla^2_{ka} + \mathcal{H}_1\, \frac{1}{s}\, d_s \Psi_I - \mathcal{H}_2\, \frac{\xi_t}{s}\, d_s(\mathrm{e}^{-s^2/s_t^2})\right] \zeta_a, \tag{3.14}$$

with $\sigma_a = \sigma/c_0^2\hat{\psi}$, $\nabla^2_{ka} = d_{ss} + s^{-1}\, d_s - s^{-2}k^2$, and the piecewise form of the basic flow is

$$\mathcal{H}_1 = \begin{cases} 1 & s, < s_l, \\ 0, & s > s_l, \end{cases} \qquad \mathcal{H}_2 = \begin{cases} 0, & s < s_l, \\ 1, & s > s_l. \end{cases} \tag{3.15a,b}$$

The numerical solution to this eigenvalue problem is based on a spectral method, which is of great accuracy and computationally economic due to exponential convergence

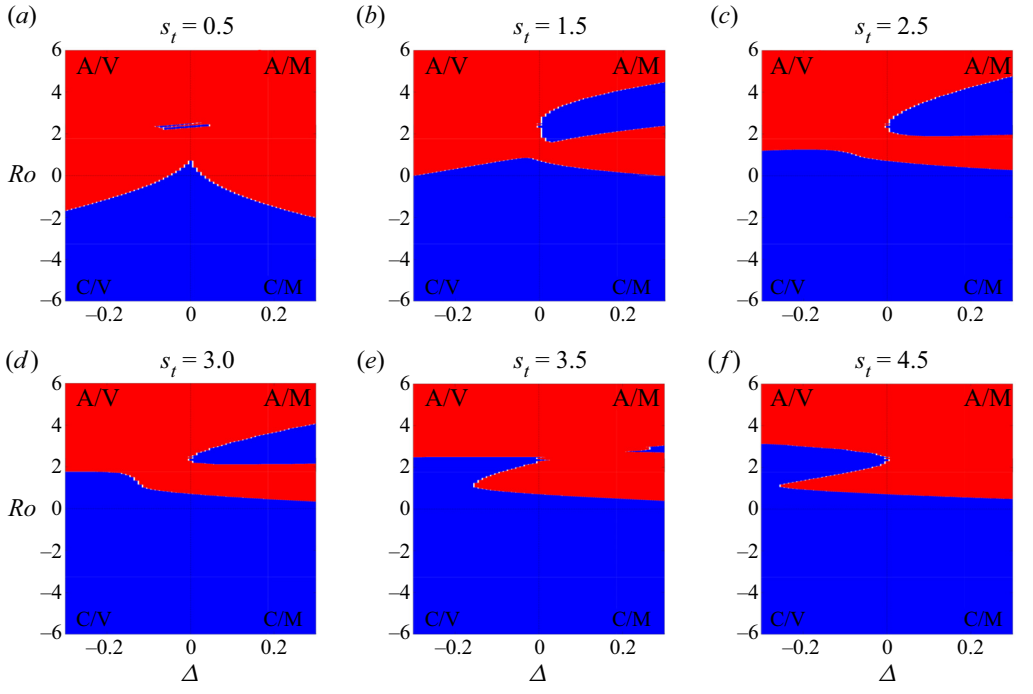

Figure 5. Dimensionless parameter space $Ro = c_0^2\hat{\psi}/f_0$ versus $\Delta = b_0/H_0$ for different width topographies s_t. The red (blue) colour indicates the vortex/topography configuration that satisfies (does not satisfy) Rayleigh's circulation criterion (3.13) for centrifugal instability.

(Orszag 1971; Yuhong 1998). Here, we will use a spectral collocation method because it is much easier to implement than the Galerkin and Tau schemes (Yuhong 1998; Trefethen 2000). The radial direction is non-uniformly discretised from 0 to 32 dimensionless units with sufficient resolution to obtain convergence. The eigenfunction is set to zero at the outer boundary. Some results were confirmed by solving the eigenvalue problem with a finite difference method. More importantly, the stability curves obtained in the study of Gent & McWilliams (1986) (their figures 2 and 5) for five different profiles of two-dimensional circular vortices were reproduced with great accuracy.

Solutions are obtained for anticyclones over mountains (A/M equivalent to C/V) and cyclones over mountains (C/M equivalent to A/V), for both $s_t = 2$ (narrow topography) and $s_t = 5$ (wide topography). The A/M configurations are chosen with integer values of parameter ξ_t, $\{\xi_t \in \mathcal{Z} \mid 1 \leq \xi_t \leq 10\}$, and the C/M with $\{\xi_t \in \mathcal{Z} \mid -10 \leq \xi_t \leq -1\}$. The solutions identify the growth rate σ_i of perturbations (2.5) with a given wavenumber k. These numbers have physical meaning only when they are integers, guaranteeing that the perturbation is azimuthally periodic. The aim is to find the wavenumber k_c with the fastest growth rate, hereafter called the characteristic wavenumber.

Figure 6 presents the stability profiles for the A/M configurations ($\xi_t > 0$). The C/M solutions ($\xi_t < 0$) are not presented because they have a zero growth rate (neutrally stable configurations). In the case of narrow topographies (figure 6*a*), the fastest growth rates have $k_c = 1$ and correspond to $\xi_t = 1$ and 2, that is, intense vortices or weak topographies. The instability with $k_c = 1$ can be associated with a slight displacement of the vortex off the centre of the topography. Dominant perturbations in vortices with $\xi_t > 2$ may have a wavenumber $k_c = 2$ but the growth rate is too small. These instability profiles are

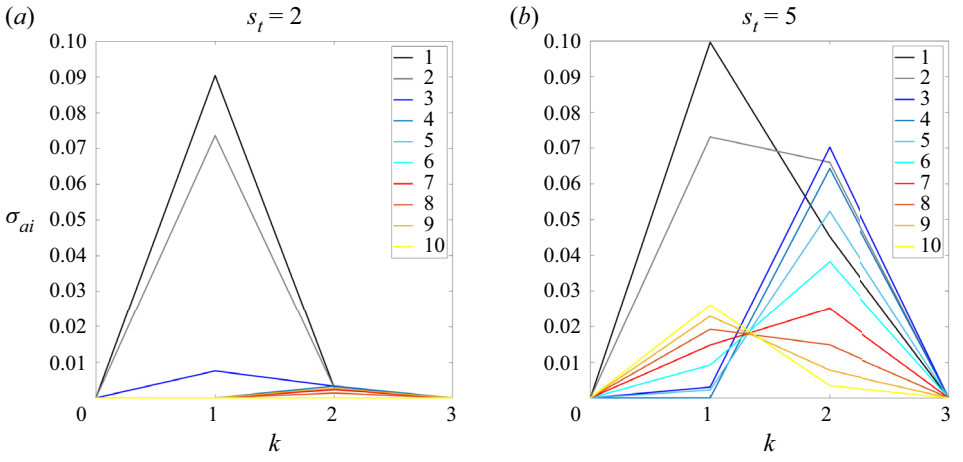

Figure 6. Instability profiles σ_{ai} (imaginary part of σ_a) versus k for cases with $\xi_t > 0$ (A/M and C/V configurations) for (*a*) narrow and (*b*) wide topographies.

obtained with 1200 Chebyshev points. In the case of wide topographies (figure 6*b*), the characteristic wavenumbers are $k_c = 1$ for $\xi_t = \{1, 2, 8 - 10\}$ and $k_c = 2$ for $\xi_t = \{3 - 7\}$, using 2500 Chebyshev points. Again, the fastest growth rate corresponds to $k_c = 1$ for $\xi_t = 1$, although other vortices show high values for $k_c = 2$.

Overall, the results from the solution of the generalised eigenvalue problem indicate that cases with $\xi_t > 0$ are unstable, whereas the cases with $\xi_t < 0$ are stable, which is in accordance with the theorems found in §§ 3.2 and 3.3 from the linear analysis.

3.6. *Numerical simulations of vortices over topography*

The evolution of circular vortices over topography is simulated numerically by solving the QG model (2.8). The numerical experiments are initialised with the circular vortices over isolated topography introduced in § 3.1. We examine the instability of A/M and C/M configurations, equivalent to the C/V and A/V cases, respectively. The vortices are liable to disturbances owing to the numerical error. We aim to detect whether the vortices are stable or unstable in long-term simulations, and in the latter case, to identify the wavenumber of the growing disturbance.

The numerical method is based on finite differences in a square grid with 513×513 points, an Arakawa scheme to discretise the nonlinear terms, and a third-order Runge–Kutta for time advancement. The non-dimensional length side of the domain is $L = 64$ or about 16 times the vortex size ($\sim$3.86), so the lateral walls are sufficiently far from the vortex. The boundary conditions are free-slip. The topography is assumed to be Gaussian. The time step is 1 % of the system's rotation period, so 100 time steps are one 'day'. The scheme has been used in numerous previous studies on vortices over a flat bottom or involving topography effects (Zavala Sansón & van Heijst 2002, 2014).

Figures 7(*a*,*b*) show the vorticity distributions at $t = 0$ and several days later for an anticyclone (bounded by the black circumference) over a narrow Gaussian mountain (magenta circumference). The vorticity profile is shown in figure 2(*b*). The results indicate that the disturbance grows and misaligns the vortex core from the origin. Hence the characteristic wavenumber is $k_c = 1$, which agrees with that predicted by the spectral method (black curve in figure 6*a*). The new structure can be characterised as an

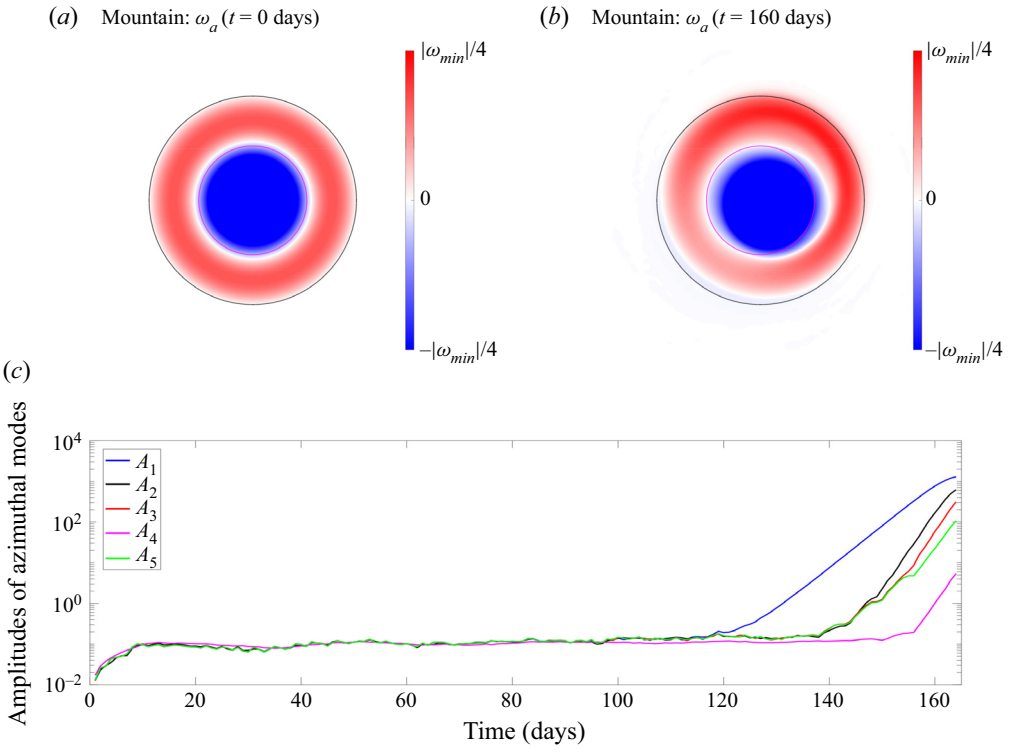

Figure 7. Numerically calculated vorticity distributions of an anticyclone over a narrow mountain $(\xi_t, s_t) = (1, 2)$ at (a) $t = 0$ days, and (b) $t = 160$ days. The limits of the colour bars are set by the peak vorticity $\omega_{min} = \min\{\omega_a\}$. (c) Time evolution of five azimuthal mode amplitudes A_k (see text). The fastest growth is for $k = 1$.

asymmetric dipolar vortex trapped over the mountain, as discussed in Gonzalez & Zavala Sansón (2021). To verify that the fastest growing mode has $k_c = 1$, we calculate the time evolution of the perturbations amplitude as done by Carton & Legras (1994). First, the vorticity perturbation is defined as

$$\omega'(r, \theta, t) = \omega(r, \theta, t) - \nabla^2 \Psi(r). \tag{3.16}$$

Second, this field is decomposed in angular modes

$$\{C_k(r, t), S_k(r, t)\} = \frac{1}{\pi} \int_0^{2\pi} \omega'(r, \theta, t)\, \{\cos(k\theta), \sin(k\theta)\}\, \mathrm{d}\theta, \tag{3.17}$$

whose amplitudes are

$$A_k(t) = \frac{1}{r_{max}} \int_0^{r_{max}} [C_k^2(r, t) + S_k^2(r, t)]\, \mathrm{d}r, \tag{3.18}$$

with $r_{max} \sim 4s_l$. Figure 7(c) presents the amplitudes time evolution for modes $k = 1 - 5$. After a brief initial period of adjustment, the amplitudes remain small and constant during 120 days, approximately. Afterwards, amplitude A_1 grows faster than the others, in agreement with the prediction of the stability analysis.

Figures 8(a) and 8(b) presents the vorticity distributions for an anticyclone over a wide Gaussian mountain (the vorticity profile is shown in figure 2d). Note that the external

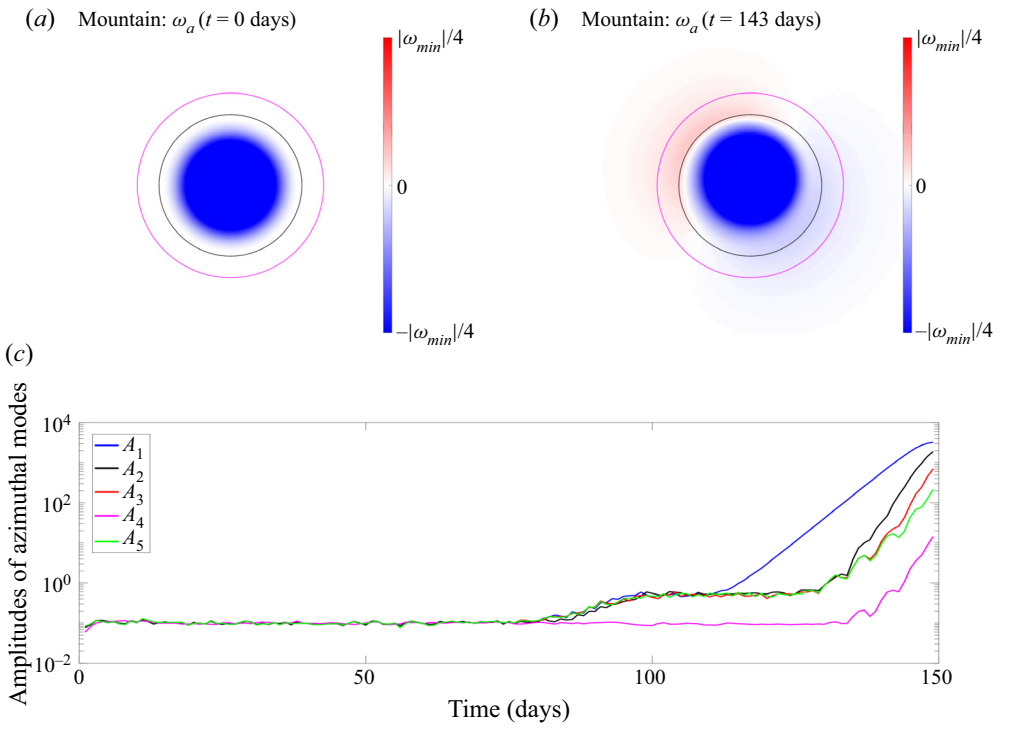

Figure 8. Numerically calculated vorticity distributions of an anticyclone over a wide mountain $(\xi_t, s_t) = (1, 5)$ at (*a*) $t = 0$ days, and (*b*) $t = 143$ days. (*c*) Time evolution of five azimuthal mode amplitudes A_k. The fastest growth is for $k = 1$.

ring of positive vorticity is very weak in comparison to the anticyclonic centre. The simulation indicates that the anticyclonic core is displaced from the origin, yielding a weak dipolar structure over the topography. This result agrees with the corresponding instability profile in figure 6(*b*) (black curve), which predicts that the fastest growing mode has a characteristic wavenumber $k_c = 1$ for this configuration. The dipole-like vortices emerging from this and the previous simulation have very different structures because of the radical differences in their initial vorticity profiles. Figure 8(*c*) presents the perturbations amplitude evolution, where it is verified that the most unstable mode is $k_c = 1$.

In figure 9, we present a case similar to that shown in figure 8, but now with $\xi_t = 3$ (a higher mountain or weaker vortex). In this case, the dominant mode has wavenumber 2, yielding an anticyclonic core with two positive vorticity satellites. The spectral solution also points out that the characteristic wavenumber is $k_c = 2$ (see the blue curve in figure 6*b*). The vortex evolution during an extended period is shown in supplementary movie 1, available at https://doi.org/10.1017/jfm.2023.153. The structure rotates as a whole in the clockwise direction around the mountain. This new vortex resembles the well-known tripolar vortices observed in laboratory experiments, which have a cyclonic core and two negative satellites, and rotate anticlockwise (Kloosterziel & van Heijst 1991). However, the vorticity distribution is notoriously different to the typical tripoles because here the core is anticyclonic, and the cyclonic satellites are very weak. Furthermore, the vortex motion

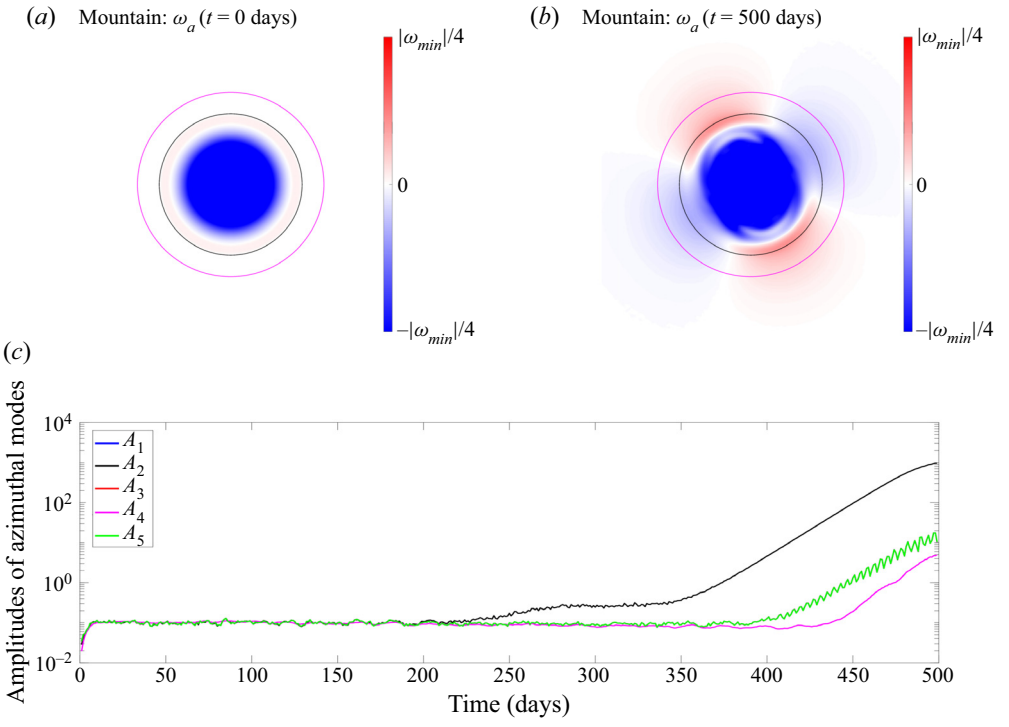

Figure 9. Numerically calculated vorticity distributions of an anticyclone over a wide mountain $(\xi_t, s_t) = (3, 5)$ at (a) $t = 0$ days, and (b) $t = 500$ days. (c) Time evolution of five azimuthal mode amplitudes A_k. The fastest growth is for $k = 2$.

is affected by the topography. The amplitudes shown in figure 9(c) verify that the most unstable mode is $k_c = 2$.

Overall, the numerical experiments indicate that most of the A/M and C/V configurations are unstable. We performed additional simulations for C/M and A/V cases, which showed that the initial vorticity distributions remained stable during very long time integrations in all cases. As an example, the evolution of a cyclone over a mountain (with $s_t = 2$, $\xi_t = -4$) during an extended period is shown in supplementary movie 2. These results are in agreement with the stability analysis, which yields a zero growth rate in these configurations, and also with the barotropic instability theorems found in §§ 3.2 and 3.3 because the necessary instability criteria are not met.

Table 2 compares the wavenumber of the fastest growing mode calculated from the eigenvalue problem and that observed in the numerical simulations. We consider narrow and wide topographies with $1 \leq \xi_t \leq 4$ (A/M or C/V) and $-4 \leq \xi_t \leq -1$ (C/M or A/V). In almost all configurations, the wavenumber obtained with both methods is the same, which suggests that the linear analysis provides reliable results. However, there are a few discrepancies, such as the two configurations with $\xi_t = 3, 4$ and $s_t = 2$ (A/M or C/V over narrow topography). The instability analysis predicts $k_c = 1$ and 2, respectively, but the numerically calculated vortices remained stable during about 600 days of simulation. The reason may be due to the small growth rate of the perturbation, as observed in figure 6(a). Probably, more simulation days would be necessary to appreciate the expected instability. Another discrepancy is the configuration with $\xi_t = 2$ and $s_t = 5$ (A/M or C/V over a

Vortex/topography configuration																
	Narrow topography								Wide topography							
s_t	2								5							
ξ_t	−4	−3	−2	−1	1	2	3	4	−4	−3	−2	−1	1	2	3	4
	k_c obtained from the eigenvalue problem															
k_c	0	0	0	0	1	1	1	2	0	0	0	0	1	1	2	2
	k_c observed in numerical simulations															
k_c	0	0	0	0	1	1	0	0	0	0	0	0	1	2	2	2

Table 2. Comparison of the characteristic wavenumber k_c predicted by the spectral solution of the generalised eigenvalue problem (§ 3.5) and that found in the numerical simulations for different vortex/topography configurations (ξ_t, s_t).

wide topography), for which the predicted wavenumber is $k_c = 1$ but the simulated vortex indicates $k_c = 2$. In this case, the difference may be due to the almost equal growth rate values for both wavenumbers, as shown in figure 6(*b*) (light grey curve).

4. Discussion and conclusions

We investigated the stability of cyclonic and anticyclonic circular vortices over isolated topographies, which can be either mountains or valleys. The results include: (i) a linear stability analysis that led to the generalised eigenvalue problem and to the incorporation of finite topography effects in classical instability theorems in the SW dynamics (§ 2); and (ii) the application of these results to QG analytical vortices over low-amplitude topography (§ 3). The latter analysis includes the spectral solution of the eigenvalue problem, and numerical simulations showing the long-term evolution of the vortices.

As a basic flow in § 3, we considered stationary, nonlinear analytical vortices over a Gaussian topography (Gonzalez & Zavala Sansón 2021). The flow/topography configurations are characterised by the dimensionless number ξ_t, which is the ratio between the relative height of the topography (whose sign indicates whether it is a mountain or a valley) and the Rossby number (also signed to distinguish cyclones and anticyclones). Thus the two dynamical configurations are comprised in cases with $\xi_t > 0$ (A/M and C/V), and $\xi_t < 0$ (A/V and C/M). The flat-bottom case is $\xi_t = 0$. A second parameter is the horizontal scale of the topography s_t.

According to the spectral solution of the generalised eigenvalue problem, the configurations A/M and C/V are unstable. The characteristic wavenumbers of the fastest growing modes are $k_c = 1$ and 2 in the range $1 \leq \xi_t \leq 10$. The largest growth rates were found for smaller ξ_t (figure 6), which indicates that the intense vortices are more unstable. In contrast, the growth rate is very small for $\xi_t \geq 3$ with narrow topography, and also for $\xi_t \geq 7$ with wide topography. This is an indication that the height of the topography may be a stabilising factor in these ξ_t ranges. On the other hand, configurations A/V and C/M ($\xi_t < 0$) are linearly stable in all cases. These results agree with the analytical and numerical study of Zhao *et al.* (2019) for the case of a Rankine vortex over a cylindrical mountain, which concluded that anticyclones are destabilised by seamounts while they are stabilised by depressions. Recently, numerical simulations carried out by Solodoch,

Stewart & McWilliams (2021) showed the formation and persistence of anticyclonic eddies over topographic depressions under a wide range of parameters, which is in agreement with the present result regarding the stability of the A/V configuration.

Long-term numerical simulations of vortices over topography agree well with the conclusions obtained from the eigenvalue problem. An aspect that stands out is that the new vortical structures emerging from unstable cases remain trapped and rotating around the topography. This behaviour resembles the asymmetric dipolar solutions obtained in Gonzalez & Zavala Sansón (2021), which rotate steadily around a seamount or valley. In Zavala Sansón & Gonzalez (2021), we reported that the residual flow over a submarine mountain after the passage of a travelling vortex is a dipolar structure that remains trapped around the tip of the mountain. A similar structure was found in laboratory experiments in a large rotating tank (Zavala Sansón *et al.* 2012).

Let us discuss the stability properties in terms of the vorticity profiles of the different vortex solutions used here. In general, the vortices have non-zero circulation, $\Gamma \neq 0$. For cases with $\xi_t > 0$ (A/M and C/V), the vorticity profiles have a core shielded by a ring with opposite vorticity (figure 2). We found that the potential vorticity gradient is zero somewhere (figure 4), so the vortices meet the modified Rayleigh and Fjørtoft instability criteria (2.15) and (2.20), respectively. Shielded vortices with $\Gamma = 0$ on a flat bottom are also barotropically unstable (Carton & McWilliams 1989; Kloosterziel & van Heijst 1991). However, in the present cases with topography and $\Gamma \neq 0$, the external ring can have much more or much less vorticity than the vortex core. As a result, the emerging 'tripolar' vortex may have a very different aspect in comparison to the traditional, flat-bottom tripoles. An example with a very weak external ring was presented in figure 9.

For cases with $\xi_t < 0$ (C/M and A/V), the vorticity profiles have definite sign, as shown in figure 3. The vorticity maximum might be either at the centre (unshielded monopoles) or at a certain radius off the origin (unshielded annuli, a vortex class that has been studied rarely). It was found that in all cases, the vorticity profiles do not meet the instability criteria, so the vortices are sufficiently stable. This result is in agreement with the well-known stable behaviour of unshielded, circular vortices found typically in laboratory experiments (Kloosterziel & van Heijst 1992). However, the stable evolution over topography contrasts with that observed for a flat bottom by Carton & McWilliams (1989), who indicated that unshielded annuli with non-zero circulation exhibit a breaking behaviour.

Finally, we discussed centrifugal instability in the presence of topography, which can be contrasted with that obtained by Kloosterziel & van Heijst (1991) for rotating flows over a flat bottom. The new criterion depends on the second radial derivative of the topographic profile and is weighted by the factor $\Delta(L_D/L)^2$; see (2.34). Roughly, we found that cyclones tend to be centrifugally stable and anticyclones unstable when seated on mountains or valleys (figure 5). Laboratory experiments or additional three-dimensional simulations would be required to test these predictions.

Supplementary movies. Supplementary movies are available at https://doi.org/10.1017/jfm.2023.153.

Acknowledgements. Comments and helpful indications from the anonymous reviewers are gratefully acknowledged. In particular, suggestions from one reviewer led us to the formulation of the instability criteria for shallow-water flows.

Funding. J.F.G. thanks the Consejo Nacional de Ciencia y Tecnología (CONACYT, México) and the Secretaría de Educación de Bogotá (Colombia) for their support.

Declaration of interests. The authors report no conflict of interest.

Author ORCIDs.
Jeasson F. Gonzalez https://orcid.org/0000-0003-3691-6443;
L. Zavala Sansón https://orcid.org/0000-0002-0419-5445.

Appendix A. Exterior field coefficients

The coefficients of the solution (3.1) are given by

$$\left.\begin{aligned} a_0 &= \frac{1}{4}\{f_{00}(4+s_l^2) + [4s_l f_{01} + 2s_l^2(\xi_t H(s_l) - f_{00})]\ln s_l - \xi_t H(s_l)\, s_l^2\},\\ a_1 &= \frac{1}{2}s_l[s_l(f_{00} - \xi_t H(s_l)) - 2f_{01}],\\ a_2 &= \frac{1}{4}(\xi_t H(s_l) - f_{00}), \end{aligned}\right\} \tag{A1}$$

where f_{00} and f_{01} are

$$\left.\begin{aligned} f_{00} &= J_0(s_l) - \xi_t\left(\frac{\pi}{2} I_2(s_l)\, J_0(s_l) - \frac{\pi}{2} Y_0(s_l)\, I_1(s_l)\right),\\ f_{01} &= \xi_t \frac{\pi}{2} Y_1(s_l)\, I_1(s_l), \end{aligned}\right\} \tag{A2}$$

and $I_1(s_l)$ and $I_2(s_l)$ are integrals involving the topography:

$$I_1(s_l) = \int_0^{s_l} H(s')\, J_0(s')\, s'\, \mathrm{d}s', \quad I_2(s_l) = \int_0^{s_l} H(s')\, Y_0(s')\, s'\, \mathrm{d}s'. \tag{A3a,b}$$

Further details about these coefficients and the properties of the background flow can be consulted in Gonzalez & Zavala Sansón (2021).

References

Carnevale, G.F. & Kloosterziel, R.C. 1994 Emergence and evolution of triangular vortices. *J. Fluid Mech.* **259**, 305–331.

Carnevale, G.F., Kloosterziel, R.C. & van Heijst, G.J.F. 1991 Propagation of barotropic vortices over topography in a rotating tank. *J. Fluid Mech.* **233**, 119–139.

Carton, X.J. & Legras, B. 1994 The life-cycle of tripoles in two-dimensional incompressible flows. *J. Fluid Mech.* **267**, 53–82.

Carton, X.J. & McWilliams, J.C. 1989 Barotropic and baroclinic instabilities of axisymmetric vortices in a quasigeostrophic model. In *Mesoscale/Synoptic Coherent Structures in Geophysical Turbulence, Liege 1988 International Colloquium on Ocean Hydrodynamics* (ed. B.M. Jamart & J.C.J. Nihoul), Elsevier Oceanographic Series, pp. 225–244. Elsevier.

Cruz Gómez, R.C., Zavala Sansón, L. & Pinilla, M.A. 2013 Generation of isolated vortices in a rotating fluid by means of an electromagnetic method. *Exp. Fluids* **54**, 1582-1–1582-12.

Cushman-Roisin, B., Heil, W.H. & Nof, D. 1985 Oscillations and rotations of elliptical warm-core rings. *J. Geophys. Res. Oceans* **90** (C6), 11756–11764.

Dewar, W.K. 2002 Baroclinic eddy interaction with isolated topography. *J. Phys. Oceanogr.* **32**, 2789–2805.

Flierl, G.R. 1988 On the instability of geostrophic vortices. *J. Fluid Mech.* **197**, 349–388.

van Geffen, J.H.G.M. & Davies, P.A. 1999 Interaction of a monopolar vortex with a topographic ridge. *Geophys. Astrophys. Fluid Dyn.* **90** (1-2), 1–41.

van Geffen, J.H.G.M. & Davies, P.A. 2000 A monopolar vortex encounters a north–south ridge or trough. *Fluid Dyn. Res.* **26**, 157–179.

Gent, P.R. & McWilliams, J.C. 1986 The instability of barotropic circular vortices. *Geophys. Astrophys. Fluid Dyn.* **35**, 209–233.

Gonzalez, J.F. & Zavala Sansón, L. 2021 Quasi-geostrophic vortex solutions over isolated topography. *J. Fluid Mech.* **915**, A64.

VAN HEIJST, G.J.F. & CLERCX, H.J.H. 2009 Laboratory modeling of geophysical vortices. *Annu. Rev. Fluid Mech.* **41**, 143–164.

VAN HEIJST, G.J.F. & KLOOSTERZIEL, R.C. 1989 Tripolar vortices in a rotating fluid. *Nature* **338**, 569–571.

HERBETTE, S., MOREL, Y. & ARHAN, M. 2002 Erosion of a surface vortex by a seamount. *J. Phys. Oceanogr.* **33**, 1664–1679.

HERBETTE, S., MOREL, Y. & ARHAN, M. 2005 Erosion of a surface vortex by a seamount on the β plane. *J. Phys. Oceanogr.* **35**, 2012–2030.

KAMENKOVICH, V.M., LEONOV, Y.P., NECHAEV, D.A., BYRNE, D.A. & GORDON, A.L. 1996 On the influence of bottom topography on the Agulhas eddy. *J. Phys. Oceanogr.* **26**, 892–912.

KLOOSTERZIEL, R.C. 1990 Barotropic vortices in a rotating fluid. PhD thesis, University of Utrecht, The Netherlands.

KLOOSTERZIEL, R.C. & VAN HEIJST, G.J.F. 1991 An experimental study of unstable barotropic vortices in a rotating fluid. *J. Fluid Mech.* **223**, 1–24.

KLOOSTERZIEL, R.C. & VAN HEIJST, G.J.F. 1992 The evolution of stable barotropic vortices in a rotating free-surface fluid. *J. Fluid Mech.* **239**, 607–629.

NYCANDER, J. & LACASCE, J. 2004 Stable and unstable vortices attached to seamounts. *J. Fluid Mech.* **507**, 71–94.

ORLANDI, P. & CARNEVALE, G.F. 1999 Evolution of isolated vortices in a rotating fluid of finite depth. *J. Fluid Mech.* **381**, 239–269.

ORSZAG, S.A. 1971 Accurate solution of the Orr–Sommerfeld stability equation. *J. Fluid Mech.* **50**, 689–703.

RABINOVICH, M., KIZNER, Z. & FLIERL, G. 2018 Bottom-topography effect on the instability of flows around a circular island. *J. Fluid Mech.* **856**, 202–227.

RABINOVICH, M., KIZNER, Z. & FLIERL, G. 2019 Barotropic annular flows, vortices and waves on a beta cone. *J. Fluid Mech.* **875**, 225–253.

RICHARDSON, P. & TYCHENSKY, A. 1998 Meddy trajectories in the Canary Basin measured during the SEMAPHORE experiment, 1993–1995. *J. Geophys. Res.* **103C**, 25029–25045.

SCHOUTEN, M.W., DE RUIJTER, W.P.M., VAN LEEUWEN, P.J. & LUTJEHARMS, J.R.E. 2000 Translation, decay and splitting of Agulhas rings in the southeastern Atlantic Ocean. *J. Geophys. Res.: Oceans* **105** (C9), 21913–21925.

SHAPIRO, G., MESCHANOV, S. & EMELIANOV, M. 1995 Mediterranean lens 'Irving' after its collision with seamounts. *Ocean Acta* **18**, 309–318.

SOLODOCH, A., STEWART, A.L. & MCWILLIAMS, J.C. 2021 Formation of anticyclones above topographic depressions. *J. Phys. Oceanogr.* **51**, 207–228.

STERN, M.E. 1975 Minimal properties of planetary eddies. *J. Mar. Res.* **33**, 1–13.

SUTYRIN, G., HERBETTE, S. & CARTON, X. 2011 Deformation and splitting of baroclinic eddies encountering a tall seamount. *Geophys. Astrophys. Fluid Dyn.* **105**, 478–505.

TREFETHEN, L.N. 2000 *Spectral Methods in Matlab*. SIAM.

TRIELING, R.R., VAN HEIJST, G.J.F. & KIZNER, Z. 2010 Laboratory experiments on multipolar vortices in a rotating fluid. *Phys. Fluids* **22**, 1–12.

VALLIS, G.K. 2017 *Atmospheric and Oceanic Fluid Dynamics*. Cambridge University Press.

VIÚDEZ, A. 2019*a* Azimuthal mode solutions of two-dimensional Euler flows and the Chaplygin–Lamb dipole. *J. Fluid Mech.* **859**, 1–12.

VIÚDEZ, A. 2019*b* Exact solutions of asymmetric baroclinic quasi-geostrophic dipoles with distributed potential vorticity. *J. Fluid Mech.* **868**, 1–13.

YUHONG, S. 1998 Collocation spectral methods in the solution of Poisson equation. PhD thesis, The University of British Columbia, Vancouver, BC.

ZAVALA SANSÓN, L. 2002 Vortex–ridge interaction in a rotating fluid. *Dyn. Atmos. Oceans* **35**, 299–325.

ZAVALA SANSÓN, L., BARBOSA AGUIAR, A.C. & VAN HEIJST, G.J.F. 2012 Horizontal and vertical motions of barotropic vortices over a submarine mountain. *J. Fluid Mech.* **695**, 173–198.

ZAVALA SANSÓN, L. & GONZALEZ, J.F. 2021 Travelling vortices over mountains and the long-term structure of the residual flow. *J. Fluid Mech.* **922**, A33.

ZAVALA SANSÓN, L. & VAN HEIJST, G.J.F. 2002 Ekman effects in a rotating flow over bottom topography. *J. Fluid Mech.* **471**, 239–255.

ZAVALA SANSÓN, L. & VAN HEIJST, G.J.F. 2014 Laboratory experiments on flows over bottom topography. In *Modeling Atmospheric and Oceanic Flows: Insights from Laboratory Experiments and Numerical Simulations* (ed. T. von Larcher & P.D. Williams), pp. 139–158. John Wiley & Sons.

ZHAO, B., CHIEUSSE-GÉRARD, E. & FLIERL, G. 2019 Influence of bottom topography on vortex stability. *J. Phys. Oceanogr.* **49**, 3199–3219.